# Tracking subsurface active weathering processes in serpentinite

Masako Tominaga*[1,2], Estefania Ortiz[1], Joshua Franz Einsle[3,4], Noah Francis Ryoichi Vento[1], Matthew O Schrenk[5], Iris Buisman[4], Isra S. Ezad[6], and Dawn Cardace [7]

(1) Texas A&M University College Station, Department of Geology and Geophysics, College Station, TX, United States
(2) Woods Hole Oceanographic Institution, Department of Geology and Geophysics, Woods Hole, MA, United States
(3) University of Glasgow, School of Geographical and Earth Sciences, Glasgow, United Kingdom
(4) University of Cambridge, Department of Earth Sciences, Cambridge, United Kingdom
(5) Michigan State University, Department of Earth and Environmental Sciences, East Lansing, MI, United States
(6) Macquarie University, Department of Earth and Environmental Sciences, North Ryde, Australia
(7) University of Rhode Island, Department of Geosciences, Narragansett, RI, United States

Corresponding author: Masako Tominaga (mtominaga@whoi.edu)

**Key Points:**

- Using micro-scale imagery of mineral phases, we identify where weathering is currently taking place in serpentine.
- Rock magnetic analyses enabled us to focus on physical boundary conditions within in situ weathering phases.

This article has been accepted for publication and undergone full peer review but has not been through the copyediting, typesetting, pagination and proofreading process, which may lead to differences between this version and the Version of Record. Please cite this article as doi: 10.1029/2020GL088472.

**Abstract**

We conducted a novel study to capture the on-going advancement of mineral weathering within a serpentinite formation by using an integrated approach of multi-scale quantitative rock magnetic analyses and nano-resolution geochemical imaging analyses. We studied a suite of rock samples from the Coast Range Ophiolite Microbial Observatory (CROMO) in California to conduct rock magnetic analyses enabling us to determine character of Fe-bearing minerals and to predict locations of reaction boundaries among various stages of weathering. QEMSCAN® and other electron micro-imagery analyses highlighted microstructural changes in amorphous minerals, and possible changes in porosity and coincides with the iron-enrichment region. This iron enrichment indicates initiation of iron (-oxides) nucleation, resulting in extremely fine gain magnetite formation. This is a newly documented mode of magnetite production in serpentinites and enhances the application of magnetite abundance as a proxy for the degree and extent of water-rock interaction in mantle peridotite and serpentinite.

**Plain Language Summary**

Accounting for the range of weathering processes on Earth enables us to understand the intertwined processes related to climate change, connect regional and global ecosystems, and evaluate the planet's chemical budget. We used quantitative rock magnetic and micro-scale analyses to capture the advancement of weathering in mineral phases, particularly in clay-rich formations and soils in core samples extracted from subsurface rock formation of the Coast Range Ophiolite Microbial Observatory where the characteristics of the clay-rich serpentinite impact microbial populations in deep biosphere. We capture weathering fronts based on information related to the physical condition of weathering phases within the boreholes and micro-scale imagery of mineral phases. By focusing on how iron-rich regions are formed in the different mineral phases and the corresponding changes where water reacts with minerals, we identify where weathering is currently taking place at a micro-scale, i.e. the foremost front of this chemical phenomena and associating changes in physical conditions (porous spaces in the rocks) that could shed a new light on the habitability of deep biosphere.

## 1. Introduction

Weathering processes occurring throughout the Earth's surface are one of the most critical components of planetary evolution. Serpentinite, as an end-member resulting from water-rock interactions within mantle peridotite formations, has been recognized as a key rock type to document the role of volumetrically significant components of the solid Earth (Beinlich et al., 2018). Quantifying and documenting weathering process in serpentinite enable us to not only understand the mechanisms that drive this component of global geochemical cycle (Beard and Hopkinson, 2000; Hattori and Guillot, 2007; Kelemen and Matter, 2008; Kelemen et al., 2011; Silantyev et al., 2012; Guillot, and Hattori 2013), but also provide insights on local soil ecosystem (Baumeister et al., 2013), and impact water quality (Oze et al., 2003; McClain et al., 2017). Despite these important implications and numerous studies on kinetics and dissolution of serpentinite-forming minerals, our knowledge on how weathering progresses within *in situ* serpentine formations has been rather limited (Ducloux et al., 1976; Caillaud et al., 2006; Baumeister et al., 2015).

The Coast Range Ophiolite Microbial Observatory (CROMO), located in northern California, is one of the rare natural laboratories that allow us to address the interactions between hydrogeology and mantle peridotite formations with various degrees of serpentinization. At

CROMO, stark seasonal contrasts in hydrological properties imply the roles of serpentine formations as physical barriers in the form of aquifers and aquitards and reactive matrices (Fig. 1) (Twing et al., 2016; Ortiz et al., 2018). In such environments, serpentine weathering has been recognized as an important determinant of soil formation and characteristics, in turn, impacting the habitability of this environment for micro- and macro-biota (e.g. Alexander, 2007; Oze et al., 2008).

We investigated serpentinite weathering processes by documenting changes in Fe-bearing minerals, prominent secondary minerals from serpentinization processes in the hydrologically distinct mantle rock formation in CROMO. We focus on the Fe-bearing mineral phases (e.g. magnetites, ilmenite) to address this aim as the weathering advancing within serpentinite equates to the mobilization and removal of Fe-bearing minerals (Ducloux et al., 1976; Caillaud et al., 2006). We used QEMSCAN® combined with a suite of rock magnetic analyses, highlighting different stages and pathways of the weathering processes downhole at a CROMO well. Our approach is novel and integrative, enabling us to push current limitation of detecting Fe-signal sources at a mineral scale.

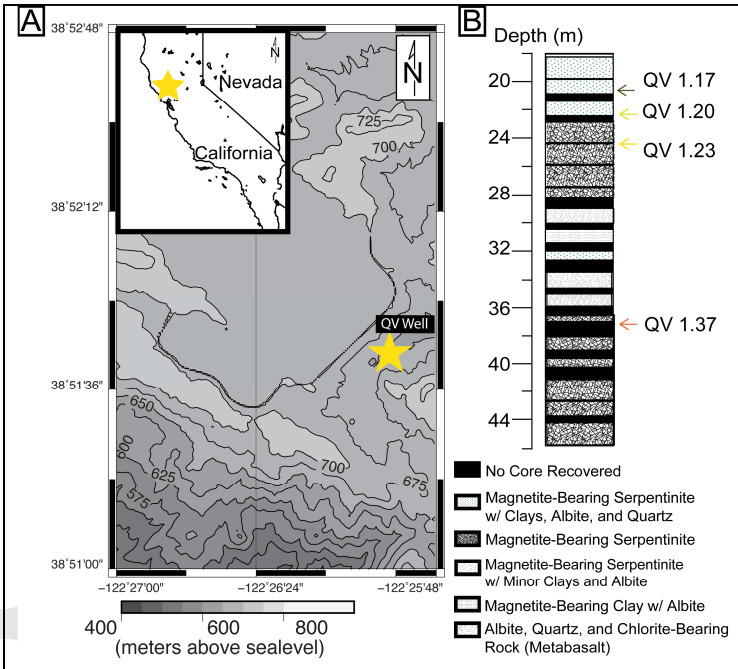


**Figure 1.** (A) Location of the Quarry Valley (QV) well and topographic map of the area surrounding the well. (B) Lithological column of the lower section of the QV well where arrows highlight the locations of the QV1.17, 1.20, 1.23, and 1.37 samples used for this study. Lithology is based on Cardace et al., 2013.

## 2. Methods and Results

*2.1 Samples and bulk rock-based descriptions in the downhole weathering sequence*

In this study, we used samples QV1.17 (17 meters below the ground level (mbgl)), QV1.20 (20 mbgl), QV1.23 (23 mbgl), and QV1.37 (37 mbgl) that are representative of four hydrologically distinctive serpentinite formations in the Quarry Valley (QV) region (38˚51.724' N, 122˚25.827' W) of the CROMO (Fig. 1)(Ortiz et al., 2018). The QV well cluster is located in a valley surrounded by a creek and serpentine hills to the north and south (Fig. 1) with hydrological architecture composed with a shallow perennial serpentinite aquifer dominated by well-drained henneke soils (Smith et al., 1989), an intermediate well-cemented serpentinite aquitard, a deep serpentine aquifer, and a deeper metamorphosed ultramafic quasi-aquiclude (Ortiz et al., 2018). Samples QV1.17, QV1.20, and QV1.23 are part of the deep serpentine

aquifer formation directly affected by the seasonal precipitation and drying cycles, whereas the QV1.37 sample is part of the deeper metamorphosed ultramafic quasi-aquiclude (Fig. 1)(Ortiz et al., 2018).

The CROMO serpentinite, from deep to shallow sites of the QV well cluster, follows the sequence of transferring Fe-bearing minerals abundant serpentinite into an assembly of clay-forming minerals by weathering (e.g. Ducloux et al., 1976; Caillaud et al., 2006). Bulk core mineralogy indicates that the QV site is dominated by a serpentine mineral, lizardite, with clay minerals, chlorite, and magnetite (Cardace et al., 2013;). Petrographic observations of QV well samples document: (1) QV1.37 is unweathered magnetite-bearing serpentine; (2) QV1.23 is serpentinite with minor clays where the rock structure and primary minerals are partially preserved; (3) QV1.20 is serpentine clays in which the texture of the rock is destroyed and further weathering has decrease the abundance of magnetic minerals; and (4) QV1.17 is serpentinite clays with albite and quartz where the magnetic carriers have been almost completely weathered away (Fig. 1).

*2.2 Detecting weathering phases in depths using rock magnetism*

To identify characteristics of major Fe-bearing minerals in the samples, we conducted a series of rock magnetic analyses at the University of Minnesota's Institute of Rock Magnetism (IRM). The experiments consist of: low-field mass-specific susceptibility measurements in an argon environment with a maximum treatment temperature of 650 K with a step of 5 K using a Kappabridge (KLY-2) (Fig. 2A); Saturation Isothermal Remnant magnetization (SIRM) measurements as a function of temperature (20-300 K), using the Quantum Design Magnetic Property Measurement System (MPMS) (Fig. 2B).

We also focus on analyzing the contribution of different magnetic grain sizes, specifically superparamagnetic (SP) and single domain (SD) magnetite (a common yet difficult to detect Fe-oxide), to the bulk susceptibility. In addition, we measured frequency dependence susceptibility using a MPMS (Fig. 2C). The following frequencies of 1, 3.2, 10, 31.6, and 99.9 Hz were measured between 10 and 330 K. To further understand the nature of Fe-bearing particles in these samples, frequency dependent susceptibility measurements were used to quantify the distribution of SP particles. The frequency-dependent susceptibility ($X_{FD}$) (percent)= ($X_{LF}$-$X_{HF}$ )/$X_{LF}$ × 100 (percent) (where $X_{LF}$ and $X_{HF}$ are the susceptibility at high and low frequencies) is used as an index in order to determine the concentration of SP particles.

Based on the reversible curves with blocking temperature at 120 K, the Verwey transition (Fig. 2A4), and Curie temperature of magnetite (Fig. 2B4), and at least consistent single to pseudo single domain grain size in particles shown by the consistency all the frequencies and $X_{FD}$ value of 0.11 (Fig. 2C4), the QV 1.37 sample, the deepest sample from the aquitard, contains magnetite. QV 1.23 sample suggests mineral alteration of magnetite to goethite (Fig. 2A3) with a small peak around 180 ˚C followed by a stronger peak around 580-595 ˚C on k(T) curve, an almost linear decrease in remanence with no Verwey transition, the SIRM curve displays, indicating the lack of magnetite in the sample (Fig. 2B3), and a wide variety of grain sizes indicated by the high $X_{FD}$ value of 16.83%. In contrast to these two deeper samples, the QV1.20 sample displays the presence of superparamagnetic particles based on the k(T) curves with a sharp decrease at 580 ˚C and slightly irreversible curves, indicating the presence of magnetite (Fig. 2A2) with the presence of superparamagnetic particles with $X_{FD}$ value of 3.17% (Fig. 2C2). Similarly, the QV 1.17 appears to show the lack of primary magnetic minerals in the sample (Fig. 2A1) based on the irreversible cooling curve with $X_{FD}$ 2.09% at room temperature.

The rock magnetic characterization clearly indicates a significant change in Fe-bearing mineral phases at depth: in the deepest aquitard represented by QV 1.37, the formation has a large contribution of single-to-multi domain size ferromagnetic minerals with little to no contribution of superparamagnetic particles, suggesting the serpentinization of mantle peridotite, either remnant or on-going, is dominant. Changes in the magnetic characteristics from ferromagnetic, single-to-multi domain size to superparamagnetic at depth appears within QV1.23 and QV1.20 samples. In particular, the QV1.20 sample exhibited mineral phases that had changed, and possibly broken down to smaller particles due to weathering, resulting in a strong contribution of SP particles in the samples.

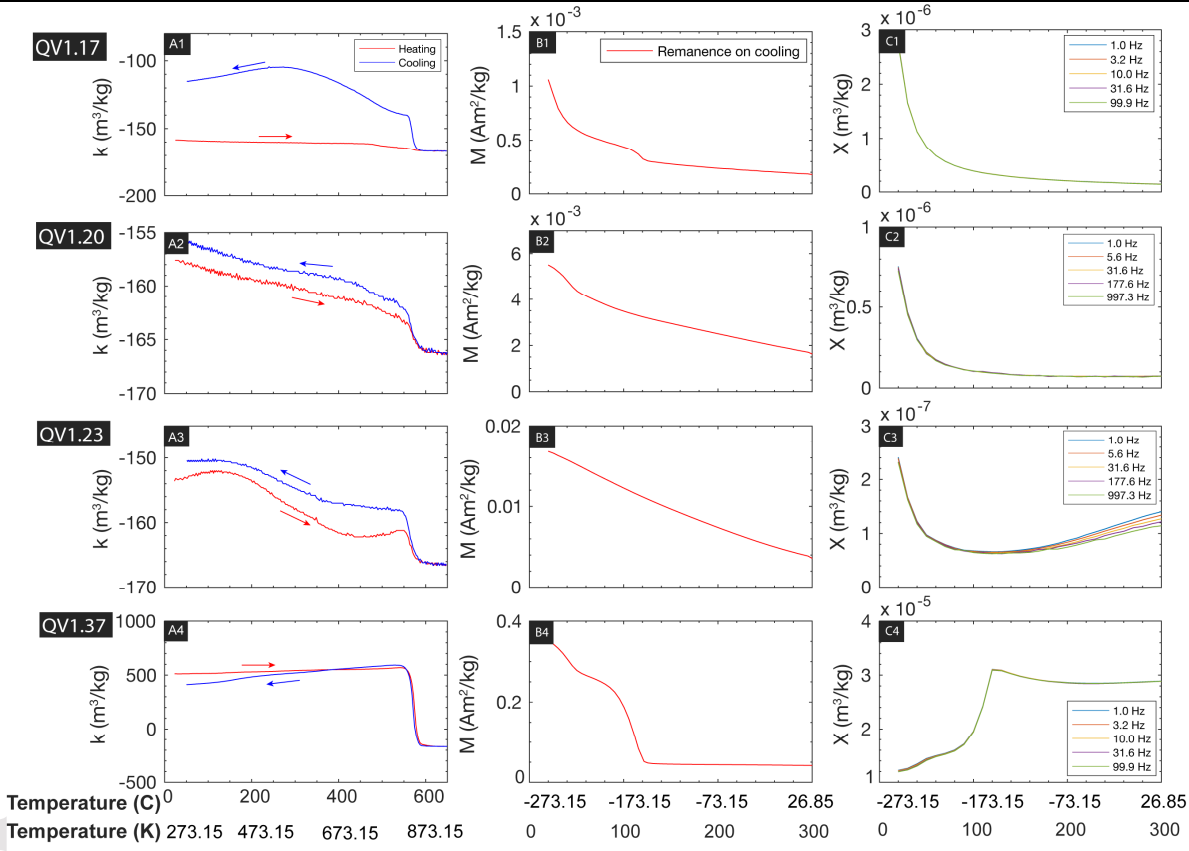


Figure 2.

**Figure 2.** Rock magnetic analyses on QV 1.17, 1.20, 1.23, and 1.37 samples from top to bottom: (A1-A4) Mass-specific magnetic susceptibility; (B1-B4) low-temperature SIRM in zero-field, and (C1-C4) frequency dependent susceptibility measurements.

*2.3 Quantitative Petrology and Micro-imagery of weathering phases*

To image the nature of weathering advancement at the finest detectable scale, we performed Quantitative Evaluation of Minerals by Scanning Electron Microscopy (QEMSCAN®) on thin sections of QV1.17, QV1.20, QV1.23, and QV1.37 samples using the Quanta 650F Scanning Electron Microscope (SEM) platform in the Earth Sciences Department, University of Cambridge. This technology enables us to visually represent the distribution of phases and minerals in these samples, as well as the iron concentrations. The instrument was

equipped with two Bruker X-Flash 6|30 Energy Dispersive Spectrometers (EDS) which, together with the back scattered electron (BSE) detector, was used to perform a fully automated spectrum acquisition and classification procedure. Analyses were performed by obtaining field-scans, providing a complete characterization of particle surfaces above a predefined electron backscatter threshold (e.g. BSE intensity is function of average atomic mass of a mineral, broadly brighter phases are denser phases). The brightness coefficients were calibrated against quartz, gold and copper. Spectra were collected at 25 kV and 10 nA with 2000 total X-ray counts per pixel at a 5 µm spacing, and compared to a Species Identification Protocol (SIP) that discriminates minerals on the basis of their characteristic X-ray and electron backscatter intensities. It should be noted that even the state-of-art QEMScan technology today has a detection limit. For example, at a 5 µm pixel size, all nanoscale features will be absorbed into the average composition and BSE intensity for any pixel (the two criteria used for QEMScan classification) demonstrating that the QEMScan technique can not directly image the superparamagnetic grain size Fe-bearing minerals, e.g. those observed in QV1.20 by rock magnetic analyses. To overcome this threshold, we examine the Fe wt% of the QEMScan mineral map data in identifying regions likely to contain these superparamagnetic grains for subsequent analyses (Fig. 3, Supplemental Information, S1-14).

QEMSCAN® mineral and Fe phase mapping results augment preliminary petrology and geochemical observations (Cardace et al., 2013; Carnevale, 2013)(Fig. 3). The QV1.37 sample is dominated by olivine and serpentine, which comprise > 90 % of its phase map (Fig. 3A, *Supp.Info. Table S1*) with magnetite and hematite (1.491 %) that are interlaced with goethite and limonite, and occur as larger, isolated grains within the overall matrix. In QV 1.23, 1.20, and 1.17 samples, little to no magnetite is detected; instead, we observed “pepper flake” sized goethite and limonite in the samples (Fig.3A and *Supp. Info. Table S1*). Sample QV1.23 also contains considerable amounts of olivine (17.2 %) and serpentine (30.6 %), as well as augite (22.6 %) and chlorite (12.6 %) (Fig. 3A and *Supp.Info. Table S1*). Particularly highlighted by this approach is the ferromagnetic (Figs. 3A and C) to superparamagnetic (Fig. 3B) signature bounded with the rock magnetic analyses in QV1.20 sample. Contrasting to the samples from deeper section, the QV1.20 marks a boundary condition where clay-forming minerals are dominantly present. These clay-forming minerals include biotite/phlogopite and feldspars, accounting for approximately 40 % of the phase map particularly for QV1.17 (Fig. 3A and *Supp.Info. Table S1*), suggesting the pervasive weathering of the QV1.17 and QV1.20 depths, starting near the QV1.20 sample depth. The extent of weathering in QV1.17 results in the almost total removal of chlorite and olivine. The origin of the feldspars may be attributed to a felsic intrusion/veins into this host mantle peridotite formation.

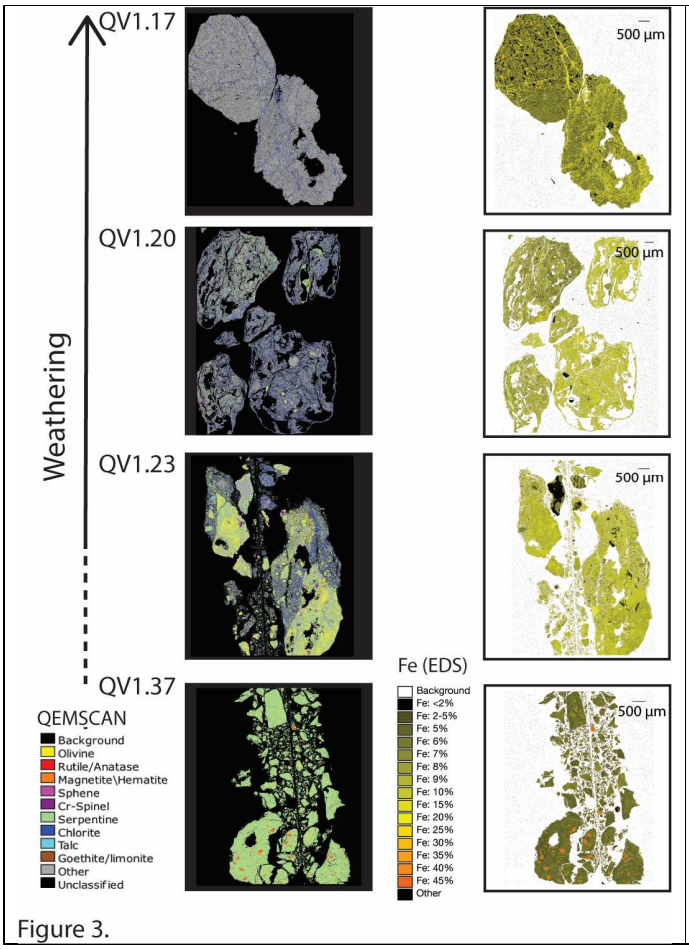

Figure 3.

**Figure 3.** Weathering profile of the QV samples (A) QV1.17, (B) QV1.20, (C) QV1.23, and (D) QV1.37. (Left) QEMSCAN® mineral phase maps. (Right) the right column displays QEMSCAN® Fe phase maps of the samples.

**Discussion: Imaging the Weathering Front in Serpentine**

In serpentinized peridotite, "dusty magnetite" or the spatter of numerous fine grain magnetites nucleating in veins has been considered to be a proxy of the onset and advancement of serpentinization within peridotite (e.g. Expedition Scientific Party, 2005; Beard et al., 2009). These magnetites/Fe-oxides can remain throughout the serpentinization processes as peridotite is altered into serpentinite (e.g. Tominaga et al., 2018). Our results from CROMO show further evolution of Fe-bearing minerals within what was originally mantle peridotite and altered by weathering processes, particularly the *re-appearance* of such fine grain, superparamagnetic size Fe-oxides (Fig. 2). Understanding the possible origins of these nano particle Fe-bearing minerals provides a clue to document the advancement of *in situ* weathering processes in serpentinite.

We first identify the region of highest iron concentration by comparing the mineral phase and Fe wt% maps of the QV1.20 sample (Fig. 4A-i), which should provide information on how this local enrichment in Fe relates to changes in mineral phases during *in situ* weathering processes. This Fe rich grain is classified as chlorite in the mineral map. The large chlorite grain encloses a bright oxide grain, later identified as ilmenite which shows the original Fe-oxide extent prior to weathering. The current oxide grain also possesses a rim of what was later identified as sphene. (mid gray in Figs. 4A-ii, -iii, and 4c).

We conducted cross-sectional analysis using a focused ion beam – scanning electron microscope (FIB-SEM) across these three phases. The FIB leverages ion beam sputtering to

selectively remove material creating a smooth cross-sectional face. The cut face is studied using high resolution BSE imaging as well as EDS mapping of the surface (Figs. 4b and c). The process for cross-sectioning the region of interest with the FIB, requires locally depositing a Pt protective cap to ensure that the top surface is not deformed by the selective sputtering process (i.e. saturating white features in Figs. 4b and c). After bulk milling is performed using a large ion beam current (1.0 nA), the cut face is polished using a lower ion beam current (73 pA) to remove material heterogeneity artifacts. Finally, the SEM collects a high-resolution BSE image (3 kV, 100 pA) of the cut face. This newly exposed cut face revels petrographic information not fully reveled in top down analysis of the thin section (Fig 4b). This cross sectioned surface reveals a three-dimensional context of recursive morphologies and porosity that are not apparent from top-down inspection alone.

To identify minerals in this cut surface (Fig. 4b), we further conducted a spatial correlation of the BSE contrast in terms of the mineral compositions of the identified using

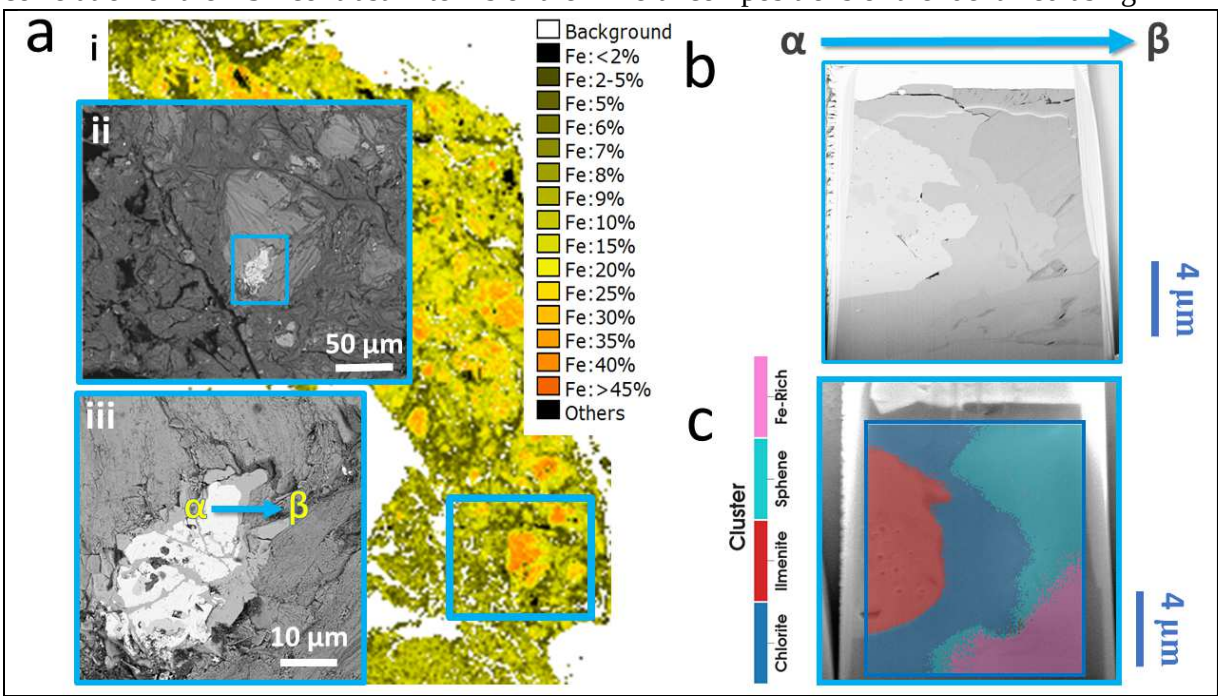


**Figure 4.** Distributions of serpentinite and iron bearing mineral phases in the QV1.20 sample. The same thin section used for the Figure 3 Left and Right panels. (a-i) Relative Fe-weight percent map from QEMScan analysis. Blue box shows region selected for cross section analysis using the FIB. (a-ii) Detail from BSE map of entire QV120 thin section. (a-iii) High normal incidence BSE micrograph of ilmenite grain and surrounding chlorite, with cross section region indicated in blue line. EDS phase map overlaid on to 20 kV BSE micro graph. (b) 3 kV BSE micrograph of cross section surface 800 nm back from EDS map. (c) Phases present are ilmenite (red), titanite (dark blue), chlorite (light blue) and magnetite (pink).

machine learning techniques (Pedregosa et al., 2011; Peña et al., 2017; Martineau et al., 2019) by collecting an EDS map (Fig 4c, beam conditions 20 kV, 1 nA) of the cross sectioned face. It should be emphasized that we use statistical tool is to oversample 10 µm wide cut face (which would have been only 2 pixels in the QEMScan maps) every 17 nm and deconvolve the extremely weak Fe signals that would be generated by superparamagnetic grains. These signals are not distinguishable using more conservative pixel sizes in the effort of minimizing beam

interaction effects (*Supp. Info.*). While the low-kV BSE image (Fig 4b) offers superior spatial imaging capabilities to the conditions used in the EDS map, direct imaging of superparamagnetic grains remains elusive. In the BSE imaging condition, we only interact with the first 5 nm (at most) of a sample compare to the roughly 1 µm interaction volume used for EDS mapping. While the EDS conditions allow us to look into the volume and find chemical signals within, the BSE only offers surface information. This surface information, especially near the bottom of the cross-section surface suffers from artifacts like FIB milling artifacts, and lower signal to noise ratio, since it is deeper into the cross-section pit. Hence, this condition unlikely resolve superparamagnetic grains on the order of 1 to 10 pixels in the BSE image.

In the resolved cross sectioned face, four distinct clusters are identified using a probabilistic fuzzy c-means clustering approach (*Supp. Info. S15 and S16*) (Martineau et al., 2019). Reprojection produces phase spectra which were individually identified as ilmenite, sphene, chlorite and a fourth Fe-oxide rich region within chlorite (Fig. 4c, *Supp. Info. S15*). The low-kV BSE image (Fig. 4b) produces a spatial resolution image where we observe microstructural relationships between ilmenite, chlorite, titanite, and Fe-rich region within the chlorite and titanite (Figs. 4a-iii, b and c, *Supp. Info. S17,S18*), especially the Fe-oxide phase corresponds with the increase of amorphous and porous material in the chlorite phase. Furthermore, we observe that the dark grey bands of amorphous materials lacing through the chlorite parent phase are more dominant in the lower region of the chlorite edge of the image than in the upper regions. This possibly indicating the direction of the weathering advancement – the porosity formation is initially formed and become more pervasive at the lower part of this mineral.

Generalizing the redox behaviors and microstructural transformations discussed by Plümper et al. (2012), it can be conjectured that these are veins with Fe-rich compositions. After the mantle peridotite is 100% serpentinized with self-cracking and advancement of alteration (Plümper et al., 2012), as the weathering advances, additional cracking mechanisms can drive and continue to operate and into further as chlorite continues to break down into clay-forming minerals. We think that the presence of these sub-50 nm magnetite grains or Fe-bearing phase are undetectable even with state-of-art micro scale imagery but significant contribution to the abundance of Fe-bearing minerals and phases through weathering of serpentinite (e.g. Fig.3). This is a newly identified mode of Fe-bearing mineral production in serpentinites by weathering of iron-oxides and possible addition to the magnetite abundance as a proxy for serpentinization and carbonation processes in mantle peridotite and serpentinite (e.g. Tominaga et al., 2017).

**Conclusion**

With a novel approach combining rock magnetic analyses and micro-imagery, we identify the active weathering front in a serpentinizing ophiolite. The weathering front in the QV1.20 serpentine sample is characterized by iron enrichment in chlorite phases at a microscale, which has originally been predicted by the rock magnetic analyses showing superparamagnetic grain distribution. The micro-imagery analyses highlighted changes in microstructural amorphous minerals possibly corresponding to the porous channel of water interacting with mineral surfaces, the region of which coincides with the iron-enrichment. This is a newly discovered mode of magnetite production in serpentinites by weathering of iron-oxides and possible addition to the magnetite abundance as a proxy for serpentinization and carbonation processes in mantle peridotite and serpentinite.

**Acknowledgement**

We thank the Institute of Rock Magnetism of University of Minnesota for Undergraduate Student Fellowships for Ortiz and Vento over two separate award years in supporting the comprehensive rock magnetic analyses, part of which contributed to this funded project. We thank the Univ. California Davis Mclaughlin Reserve – for their help and accommodation during the multiple seasons of field work at CROMO. We thank M. Kubo for his ever cheerful leadership and students mentoring in CROMO over multiple seasons that made this collaborative work productive and joyful. The data are digitally archived in cloud-base storage and accessible upon request to the authors. This study was supported by Rock Powered Life grant (NASA Astrobiology Institute) NNA15BB02A. J.F.E. acknowledges funding under ERC Advanced Grant 320750-Nanopaleomagnetism.

**Data availability**

Datasets for this research, supplementary information files, python code is available in publicly accessible GitHub/Zenedo repository via
DOI 10.5281/zenodo.4391090**.**

**References**

Alexander, E. B., R. G. Coleman, T. Keeler-Wolf, and S. Harrison, 2007, Serpentine Geology of Western North America: Geology, Soils, and Vegetation, 512 pages, Oxford University Press, New York.

Beinlich, A., H. Austrheim, V. Mavromatis, B. Grguric, C. V. Putnis, and A. Putnis, 2018, Peridotite weathering is the missing ingredient of Earth's continental crust composition, Nature Comm., 9, 634, https://doi.org/10.1038/s41467-018-03039-9.

Beard, J. S., and L. Hopkinson, 2000. A fossil, serpentinization-related hydrothermal vent, Ocean Drilling Program Leg 173, Site 1068 (Iberia Abyssal Plain): Some aspects of mineral and fluid chemistry. *Journal of Geophysical Research: Solid Earth*, *105*(B7), 16527-16539.

Butler, R. F., 1998, Paleomagnetism: Magnetic domains to geologic terranes. *Electronic edition*, *23*.

Cardace, D., T. Hoehler, T. McCollom, M. Schrenk, D. Carnevale, M. Kubo, and K. Twing, 2013, Establishment of the Coast Range ophiolite microbial observatory (CROMO): drilling objectives and preliminary outcomes: Scientific Drilling, *Sci. Dril.*, *16*, 45–55.

Carnevale, D.C., 2013, Carbon sequestration potential of the coast range ophiolite in California, M.S. thesis, University of Rhode Island, Kingston, Rhode Island.

Caillaud, J., D. Proust, and D. Righi, 2006, Weathering sequences of rock-forming minerals in a serpentinite: Influence of microsystems on clay mineralogy, *Clay and Clay Mineral.*, 54, 1, 87-100.

Ducloux, J., A. Meunier, and B. Velde, 1976, Smectite, chlorite and a regular interlayerd chlorite-vermiculite in soils developed on a small serpentinite body massif central, France, 1976, *Clay Minerals*, 11, 121-135.

Guillot, S., and K. Hattori, K, 2013, Serpentinites: essential roles in geodynamics, arc volcanism, sustainable development, and the origin of life. *Elements*, *9*, 95-98.

Hattori, K. H., and S. Guillot, 2007, Geochemical character of serpentinites associated with high- to ultrahigh-pressure metamorphic rocks in the Alps, Cuba, and the Himalayas: Recycling of elements in subduction zones, *Geochem. Geophys. Geosyst.*, 8, Q09010, doi: 10.1029/2007GC001594.

Holzer, L., F. Indutnyi, P. H. Gasser, B. Munch, and M. Wegmann, 2004, Three-dimensional analysis of porous BaTiO3 ceramics using FIB nanotomography, *Jour. Microscopy*, 216, 84–95, doi:10.1111/j.0022-2720.2004.01397.x

Kelemen, P. B., and J. Matter, 2008, In situ carbonation of peridotite for CO2 storage. *Proceedings of the National Academy of Sciences*, *105*, 17295-17300.

Kelemen, P. B., J. Matter, E. E. Streit, J. F. Rudge, W. B. Curry, and J. Blusztajn, 2011, Rates and mechanisms of mineral carbonation in peridotite: natural processes and recipes for enhanced, in situ CO2 capture and storage. *Ann. Rev. Earth Planet. Sci.*, *39*, 545-576.

Klein, F., S. E. Humphris, W. Guo, F. Schubotz, E. M. Schwarzenbach, and W. D. Orsi, 2015, Fluid mixing and the deep biosphere of a fossil Lost City-type hydrothermal system at the Iberia Margin. *Proceed. Nat. Acad. Sci.*, *112*, 12036-12041.

Martineau, B. H., D. N., Johnstone, A. T. J. van Helvoort, P. A. Midgley, and A. S. Eggeman, 2019, Unsupervised machine learning applied to scanning precession electron diffraction data, *Adv. Struct. Chem. Imaging* **5**, 3.

Nylese, T., and R. Anderhalt, 2014, Advanced Materials Characterization with Full-Spectrum Phase Mapping, *Micro. Today, 22*, 18-23, doi:10.1017/S1551929514000157

Ortiz, E., M. Tominaga, D. Cardace, M. O. Schrenk, T. M. Hoehler, M. D. Kubo, and D. F. Rucker, 2018, Geophysical characterization of serpentinite hosted hydrogeology at the McLaughlin Natural Reserve, Coast Range Ophiolite, *Geochem. Geophys. Geosys.*, 19, 114–131. https://doi.org/10.1002/2017GC007001.

Pedregosa, F., G. Varoquaux, A. Gramfort, V. Mitchel, B. Thirion, O. Grisel, M. Blondel, A. Müller, J. Nothman, G. Louppe, P. Prettenhofer, R. Weiss, V. Dubourg, J. Vanderplas, A. Passos, D. Cournapeau, M. Brucher, M. Perrot, É. Duchesnay, 2011, Scikit-learn: Machine Learning in Python, *J. Mach. Learn. Res.*, 12, 2825–2830.

Peña, F. de la, T. Ostasevicius, V. T. Fauske, P. Burdet, P. Jokubauskas, M. Nord, M. Sarahan, E. Prestat, D. N. Johnstone, J. Taillon, J. Caron, T. Furnival. K. E. MacArthur, A. Eljarrat, S. Mazzucco, V. Migunov, T. Asrholt, M. Walls, F. Winkler, G. Donval, B. Martineau, A. Garmannslund, L.-F. Zagonel, and I. Iyengar , 2017, *HyperSpy* 1.1.2. doi:10.5281/ZENODO.240660.

Plümper, O., A. Royne, A. Magraso, and B. Jamtveit, 2012, The interface-scale mechanism of reaction-induced fracturing during serpentinization, *Geology*, 40, 1103–1106.

Silantyev, S. A., A. A. Novoselov, E. A. Krasnova, M. V. Portnyagin, F. Hauff, and R. Werner, 2012, Silicification of peridotites at the stalemate fracture zone (Northwestern Pacific): Reconstruction of the conditions of low-temperature weathering and tectonic interpretation, *Petrology*, *20*, 21-39.

Smith, D. W., and W. D. Broderson, 1989, *Soil survey of Lake County, California*, 456 pages, The United States Soil Conservation Service.

Tominaga, M., A. Beinlich, E. A. Lima, M. A. Tivey, B. A. Hampton, B. Weiss, and Y. Harigane, 2017, Multi-scale magnetic mapping of serpentinite carbonation, *Nature Comm.*, 8, doi.org/10.1038/s41467-017-01610-4

Twing, K. I., W. J. Brazelton, M. D. Y. Kubo, A. J. Hyer, D. Cardace, T. M. Hoehler, T. M. McCollom, and M. O. Schrenk, 2017, *Front. Microbio.*, doi.org/10.3389/fmicb.2017.00308

Van Der Walt, S., J. L. Schönberger, J. Nunez-Iglesias, F. Boulogne, J. D. Warner, N. Yager, E. Gouillart, and T. Yu, 2014, Scikit-image: Image processing in python, *PeerJ*, https://doi.org/10.7717/peerj.453

Whitney, D. L., and B. W. Evans, 2010, Abbreviations for names of rock-forming minerals. Am. Mineral. 95, 185–187.